Rational design process for gas turbine exhaust to supercritical CO_2 waste heat recovery heat exchanger using topology optimization

Nosherwan Adil[1], Sebastian N Dryepondt[2], Anand Kulkarni[3], Patrick J Geoghegan[4], Xiang Zhang[1], Abdulaziz Alkandari[1], Alexander S Rattner[1]*

[1]The Pennsylvania State University, State College, PA, 16802, USA
[2]Oak Ridge National Laboratory, Oak Ridge, TN, 37830, USA
[3]Siemens Corporation, Charlotte, North Carolina, 28273, USA
[4]Oregon State University, Corvallis, OR, 97331, USA
*Corresponding Author: 236A Reber Building, University Park, PA, 16802, USA
Email: Alex.Rattner@psu.edu

Abstract

Advances in additive manufacturing (AM) technologies and topology optimization methodologies are enabling sophisticated novel designs for heat exchanger performance. These tools have been demonstrated for development of high-performance heat sinks considering local or component-level performance factors (*e.g.*, heat transfer per volume). To leverage such capabilities in larger-scale energy systems, structured design methodologies are needed that consider system-level factors, such as production cost, cycle-level efficiency, and operational constraints. This study seeks to develop and assess a rational approach for designing thermo-economically optimal heat exchangers for such applications. The methodology is illustrated through development of the Primary Heat Exchanger (PHX) for a supercritical carbon dioxide (sCO_2) power cycle recovering exhaust heat from a 6 MW-scale natural gas turbine. The proposed approach begins with a detailed thermodynamic cycle model, which is then extended to account for techno-economics. Next, an optimal PHX heat transfer capacity target is identified, and a high-level geometry is selected based on operating characteristics. This geometry is then divided into repeating 2D prismatic unit cells, for which topology optimization is applied to identify high-performance heat transfer geometries. A key aspect of this process is that the unit cell geometries are optimized using the total PHX mass as the objective function, which represents a surrogate for production cost. This leads to distinct designs compared with approaches that optimize local heat transfer and flow resistance factors. A second topology-optimized design is developed using a representative local thermal-fluid performance objective function and is found to require 1.6× the mass of the design generated with the system-level techno-economic objective for the same unit cell size. Conventional-type PHX designs with simple longitudinally finned tubes are developed for comparison, and are found to require total masses 1.5× or greater than the design obtained with the proposed process. Integrating this approach with detailed additive manufacturing costing models and experimentally validated fabrication constraints can yield a streamlined workflow for HX design for future energy systems.

Keywords

Topology optimization; Additive manufacturing; Heat exchanger; Supercritical carbon dioxide;

1 Introduction

1.1 Background and present investigation

Topology optimization (TO) methods, enabled by advances in metal additive manufacturing (AM), are increasingly being explored for development of high-performance heat transfer equipment. TO is an algorithmic process of material and void placement within a design domain to minimize objective functions within constraints. TO algorithms can pair well with many AM processes, which offer greater freedom in geometry than conventional fabrication. Recent investigations have sought to leverage TO for high-value applications, such as aerospace [1] or electronics thermal management [2]. In these fields, thermal-hydraulic performance gains can justify high AM production costs. In such applications, the driving objective function is often to maximize local thermal hydraulic performance factors, such as heat transfer per volume or heat transfer per pressure drop.

However, as costs of metal AM continue to decline, waste heat recovery (WHR) heat exchangers leveraging TO geometries, may soon become commercially viable. In many WHR applications, heat is recovered from high temperature and potentially corrosive exhaust gas streams, necessitating the use of expensive high-performance materials (*e.g.*, Ti or Ni alloys) for primary heat exchangers (PHX). Compared with conventional HX manufacturing processes designed for specific materials (*e.g.*, sheet metal stamping, soldering), current AM equipment can support diverse build materials. WHR systems are often designed for specific industrial plants and applications; therefore, hardware is sourced as prototypes or at low order volumes. With conventional HX fabrication processes, specialized fixtures and tooling can incur high setup costs and lead times for WHR equipment. AM can offer minimal setup costs, provided that typical build constraints are satisfied.

Design for WHR must address different considerations than in aerospace or electronics thermal management fields. First, industrial WHR systems are typically stationary and larger package volumes can often be tolerated. Transport intensity (*i.e.*, heat transfer per volume) is less critical than in aerospace and thermal management applications. Further, WHR systems are driven by effectively free energy sources. System economics are thus dominated by capital costs of major components rather than raw efficiency or specific power. Considering these distinct objectives, the present study proposes a procedure to guide the design of specialized industrial WHR PHXs that leverage TO geometries enabled by AM.

The proposed approach proceeds through the following stages (Figure 1):

1. WHR cycle-level thermodynamic modeling is performed for specified operating conditions, and system-level constraints are identified. Optimizing over remaining degrees of freedom, overall system technical performance is mapped to PHX capacity (*e.g.*, net WHR power output vs. PHX overall heat transfer coefficient (UA)).
2. A techno-economic analysis is performed, using thermodynamic data from Stage 1 and cost inputs (*e.g.*, value of output power, hardware cost curves). This yields a target PHX capacity (UA) that maximizes system net present value.
3. A high-level geometry definition is then formed for the PHX, considering thermal and flow factors for the waste heat and coupling fluid streams.

4. PHX geometry is improved through topology optimization, seeking to minimize capital cost, while satisfying required heat transfer capacity and other constraints, such as allowed pressure drop.

The overall process may be iterated to approach techno-economically optimal PHX designs. In particular, sensitivity of PHX UA to capital cost obtained in Stage 4 can replace generic component cost curves employed in Stage 2. The proposed methodology is illustrated here through the design of a PHX that captures waste heat from the exhaust of a microturbine (482°C inlet) and supplies it to a supercritical CO_2 bottoming cycle.

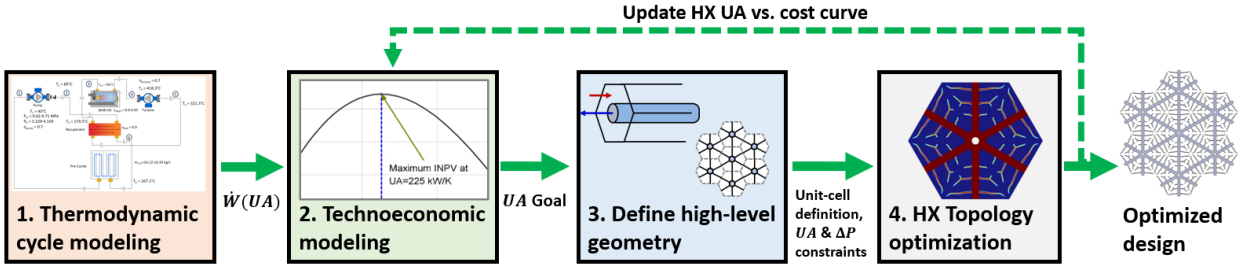

Figure 1: Summary flow chart of the proposed waste heat recovery heat exchanger topology optimization procedure

The core concept of optimizing HX size and geometry for techno-economic system-level goals has been demonstrated for a range of energy systems. Some prior studies have assumed fixed overall heat transfer coefficients (U) and sought to vary HX area to maximize system net present value for applications including organic Rankine cycles [3], natural gas liquefaction [4], and CO_2 capture [5]. More detailed HX economic optimization studies have also considered geometry parameters as design variables. Such studies have employed analytic transport correlations [6], [7] or full computational fluid dynamics (CFD) simulations [8], [9] to predict effects of geometry parameters on HX performance. However, to our knowledge all prior HX techno-economic optimization studies have considered few, discrete, geometric design variables, such as tube diameters, fin pitch, or baffle angles [10]. The present investigation seeks to extend such approaches to topology-optimization driven design of HXs with thousands of design degrees-of-freedom.

1.2 Prior research on topology optimization of heat transfer equipment

AM coupled with topology optimization has been explored in recent investigations seeking to develop high-performance heat transfer equipment. Haertel *et. al* [2] used a density-based topology optimization scheme to maximize the conductance (inverse of thermal resistance between the two fluids) for an air-cooled heat exchanger for a prescribed pressure drop and air-side temperature change across the heat exchanger. They found that their topology optimized designs yielded 71% more conductance per unit volume, than the conventional designs.

Lange *et. al* [11] performed related investigations, and designed a heat sink using topology optimization and parametric studies, with the objective of minimizing the temperature of a cooled component. Their optimized design required $1/4^{th}$ of the mass of a conventional heat sink.

In another study, Haertel *et. al* [12] used topology optimization to refine heat sinks, employing a two-dimensional forced convection model. In their study, the objective was to minimize the heat sink temperature for a prescribed pressure drop and fixed heat generation. A 2D heat sink model with constant heat production and a density-based topology optimization model [13] was evaluated.

Kobayashi *et. al* [14] developed a novel winglet design of a fin-and-tube heat exchanger guided by topology optimization. Their optimization problem was formulated to maximize heat extraction by winglets in a two-dimensional simplified model for low Reynolds number flows. A variety of fin pattern configurations were obtained with topology optimization, and the manufacturable fin pattern adapted from the best candidate had up to 16% higher quality factor (ratio of Colburn *j* factor to friction factor) compared with the fins with rectangular winglets pairs.

Saviers *et. al* [15] applied a topology optimization methodology for developing a prototype heat exchanger design for a sCO_2 power cycle recuperator. In experiments, they measured a 50% reduction in pressure loss and a 10% increase in heat transfer compared with a baseline design having the same wall thickness, external space dimensions, and fluid flow routing.

Mekki *et al*. [1] recently developed a genetic-algorithm based topology optimization approach to enhance fin geometries for aerospace application heat exchangers. In their computational fluid dynamics simulations, they achieved an 89% enhancement over baseline geometries for an objective function of fitness $F = Q/(\Delta P)_f^{1/3}$ – the ratio of heat transfer to a fractional power of frictional pressure drop.

Most of these studies have employed local thermal-fluid performance metrics to guide optimization, such as *heat transfer per volume*, *heat transfer per pressure drop*, or *quality factor*. However, designs that optimize such metrics may not necessarily perform best on system-level factors relevant to WHR applications, such as cycle-level efficiency or net present value. The approach proposed here is distinct in that the initial sizing and subsequent topology optimization stages target *system-level economic* criteria, illustrated for a WHR sCO_2 power cycle.

1.3 Overview of sCO_2 power cycles and application

Supercritical CO_2 power cycles have similar cycle-level working principles to closed-loop Brayton cycles, but can employ comparatively compact hardware due to the high fluid density at the 10 – 30 MPa working pressures. These cycles can achieve high thermal efficiency at relatively low turbine inlet temperatures (450°C – 750°C) because they have the advantages of both Brayton cycles, with high specific turbine work and effective recuperation, and Rankine cycles, with low compression back-work at near-critical conditions [16]. CO_2 is non-toxic, environmentally benign, and has favorable heat and mass transport properties at working pressures. The global warming potential of CO_2 is 1,000 – 3,000× lower than other hydrocarbons or HFC working fluids [17]. sCO_2 can also effectively capture waste heat from sources with temperature glides, such as turbine exhaust or other gases. Perceived challenges to commercializing sCO_2 cycles include the relatively high operating pressures and temperatures

[18]. Still, the potential benefits of sCO_2 power cycles have motivated intense research and development efforts in recent years.

A variety of sCO_2 power cycle configurations have been proposed, including simple recuperated cycles, recompression cycles, recompression with intercooling, recompression with partial cooling, and recompression with main-compressor intercooling [19]. To illustrate the proposed HX design process, a simple recuperated sCO_2 power cycle is assumed here, sized for WHR from a representative ~6 MW gas turbine, as may be used in campus- or industrial-scale power generation.

2 Design methodology

In this section, the proposed 4-stage WHR HX design methodology (Section 1.1) is illustrated in detail for a conceptual sCO2 power cycle application.

2.1 System-level analysis and identification of design constraints and objectives

The proposed HX design process begins with a system level-model of the power generation cycle. Here, a simple recuperated sCO_2 power cycle is assumed with typical turbomachinery performance levels ($\eta_{comp} = \eta_{turb} = 70\%$), heat rejection to the ambient with a compressor inlet temperature of 40°C, effective recuperation ($\varepsilon_{RHX} = 0.9$), and a counterflow PHX as shown in Figure 2. The gas turbine exhaust gas enters the PHX at 482°C. A allowed gas turbine back pressure allowance of 8,000 Pa is assumed. Based on these assumptions, the sCO_2 power cycle has four main remaining degrees-of-freedom in design and operating conditions: (1) low-side pressure (P_L), (2) high-side pressure (P_H), (3) sCO_2 circulation rate ($\dot{m}_{CO2}$), and (4) primary heat exchanger capacity (UA_{PHX}) – *the component under design*.

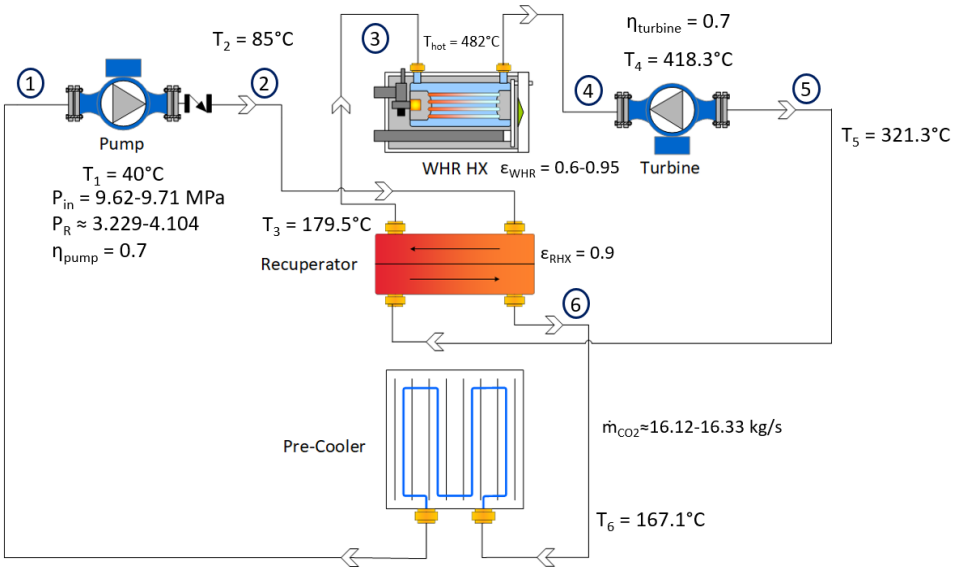

Figure 2: Diagram of the single stage recuperated sCO_2 power cycle recovering gas turbine exhaust heat

For this sCO_2 power cycle, optimal values of parameters 1-3 can be identified for any given value of UA_{PHX} to maximize power output (Figure 3). The PHX capital cost can be assumed to scale with UA_{PHX}. Then, an economic model and corresponding assumptions can be applied to identify an optimal target UA_{PHX}. A PHX cost-curve model [20] is adopted (Section 2.2.), which leads to a target UA_{PHX} = 225 kW K^{-1}. The corresponding optimal values of $\dot{m}_{CO2}$, P_H, and T_3 (sCO_2 inlet temperature to PHX) will be used in the detailed HX design (Sections 2.3 – 2.5) are summarized in Table 1.

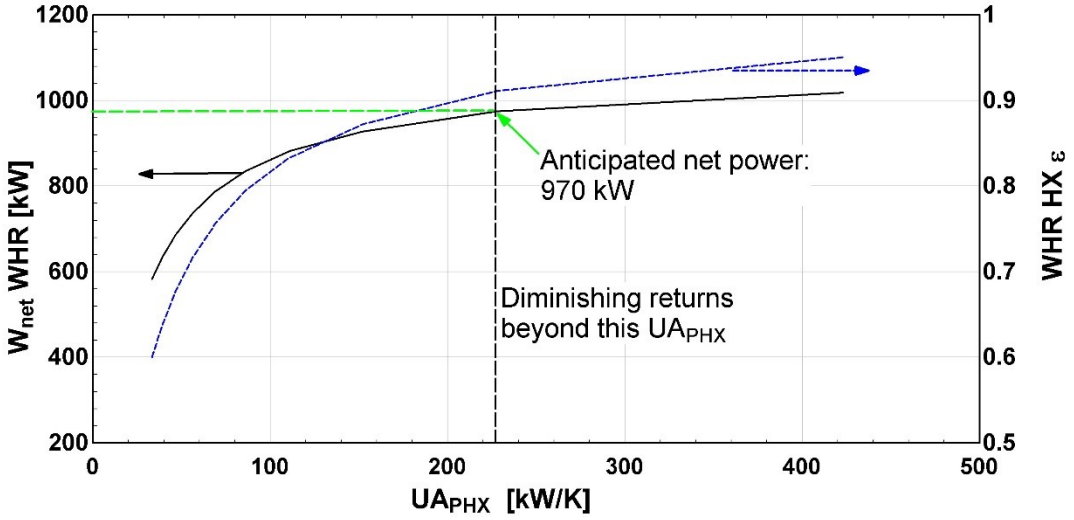

Figure 3: Maximized sCO_2 cycle power output vs. PHX capacity (UA_{PHX}). Values for low-side pressure (P_L), high-side pressure (P_H), and sCO_2 mass flow rate are varied for each UA value to maximize power output.

Table 1: Input parameters for detailed PHX design

Parameter	**Value**
CO_2 mass flow rate ($\dot{m}_{CO2}$)	16.4 kg s^{-1}
Exhaust mass flow rate ($\dot{m}_{ex}$)	21.1 kg s^{-1}
HX effectiveness (ε_{HX})	0.88
CO_2 high-side pressure (P_H)	31 MPa
CO_2 inlet temperature (T_3)	179.5°C

2.2 Economic model of the PHX and sCO_2 cycle

The capital cost of the PHX is estimated using typical costing methods for an air-cooled heat exchanger [21]:

$$C_{HX} = \frac{740}{397}(B_1 + B_2 F_M F_P) F_s C_{HX}^0 \quad (1)$$

Here, C_{HX} is the heat exchanger cost in USD, B_1 and B_2 are constants for the equipment type, F_M is the material cost factor (stainless steel assumed here), F_P is the pressure factor, F_S is an additional cost factor that accounts for material, piping, labor, etc., and C_{HX}^0 is the estimated cost of an equivalent heat exchanger made from carbon steel operating at ambient pressure in 2001 USD. Stainless steel is selected as the HX material in this study, considering the higher operating temperature and potentially corrosive exhaust gas stream. The cost obtained from Eqn. 1 is scaled to 2019 USD using the ratio of CEPCI for the relevant years (397 for 2001; 740 for 2019). The base cost estimate for the carbon steel HX is given by Eqn. 2:

$$C_{HX}^0 = \begin{cases} 10^{(K_1 + K_2 log A + K_3 [log A]^2)}, & A < 10{,}000 \text{ m}^2 \\ \dfrac{A}{1{,}000} 10^{(K_1 + K_2 log 10000 + K_3 [log 10000]^2)}, & A > 10{,}000 \text{ m}^2 \end{cases} \quad (2)$$

Here K_1, K_2 and K_3 are constants for the heat exchanger type, and A is the area in m^2, over which heat exchange occurs in the heat exchanger. The value of all constants in the previous equations are given in Table 2 [21].

The pressure factor is given by Eqn. 3 [22].

$$F_P = 0.939 P^{0.04759} \quad (3)$$

Here, P is the fluid pressure in bar.

Table 2: Constants for PHX cost projection

F_S	B_1	B_2	F_M	K_1	K_2	K_3
1.7	0.96	1.21	2.9	4.0336	0.2341	0.0497

The values for the overall heat transfer coefficient, U ($UA = U \times A$), may vary depending on working fluids and HX design specifics. Here, U = 300 W m^{-2} K^{-1} is estimated based on data for heat exchangers operating with air and fluids with similar properties to sCO_2 [20].

For the purposes of this PHX design study, it is assumed that the costs and efficiencies of all other WHR system components are approximately fixed. In a final design stage, effects of varying characteristics of such components could be propagated. Given this assumption, an Incremental Net Present Value (INPV) approach can be used to select a target PHX UA value. INPV is the net value in present terms, considering all cash inflows and outflows over the equipment lifetime, relative to a baseline plant design (subscript b). INPV is given by Eqn. 4 in USD:

$$INPV = N(A_e - A_{e,b}) - (C_{HX} - C_{HX,b}) \quad (4)$$

Here, N is the years of lifetime (assumed 10 years in this study). A_e is the electricity value produced per year in USD for a specific PHX UA, and $A_{e,b}$ is the electricity value produced per year in USD for a plant with an arbitrary baseline PHX UA (100 kW K^{-1}). Similarly, C_{HX} and

$C_{HX,b}$ are the capital costs for plants with PHXs at specific and baseline UA values, respectively. The WHR plant is assumed to operate for 8,760 hours each year, and the value of electricity is assumed to be 0.102 USD kWh^{-1}. The optimal PHX UA value that maximizes INPV is 225 kW K^{-1} (Figure 4), which becomes a design constraint in the next steps.

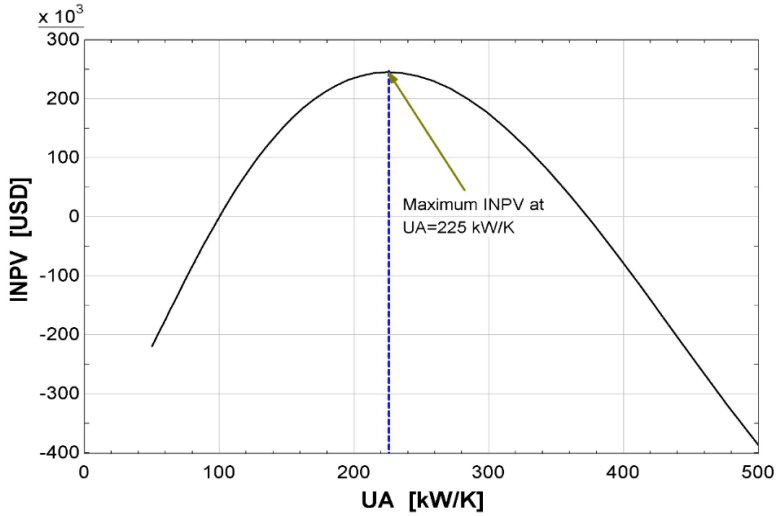

Figure 4: Incremental net present value (INPV) of waste heat recovery cycle vs. primary heat exchanger UA

It should be noted that the HX design obtained through the proposed process may be unconventional and may not conform to the assumed costing curve (Eqns. 1-3). Therefore, the overall design approach may be iterative in the sense that this cycle-level thermo-economic stage could be updated based on the final PHX specifications, and subsequent design steps could be repeated.

2.3 High-level geometry definition for topology optimization

In the counterflow PHX application, the exhaust gas volume flow rate is greater than that of the sCO_2 stream by ~800×. The exhaust gas pressure drop constraint is relatively low to ensure proper gas turbine operation (ΔP_{max} = 8,000 Pa). Thus, a high performing PHX design should have much greater exhaust-side flow area than sCO_2 flow area. In actuality, there may be a range of acceptable ΔP values that would incur tradeoffs between the gas turbine and WHR cycles, but a single representative value is assumed here for illustration.

Conceptually, minimizing thermal resistance between the two streams may be achieved by limiting the heat transfer distance between material elements of the two streams through any HX cross-section. From a geometric perspective, this motivates a design with circular unit-cells with a small CO_2 channel in the core and exhaust gas flow in the annulus. In this PHX design, such circular unit cells are reduced to hexagons, for 100% packing density in the HX cross-section, reducing component size and mass. Circular unit cells would be separated by inactive gaps of 9% area. Designs can be further constrained by assuming 12-way radial symmetry in each hexagonal

unit cell (triangular sub-unit-cells, SUC). For this WHR application, the design problem reduces to optimizing the geometry of a repeating triangular SUC (Figure 5).

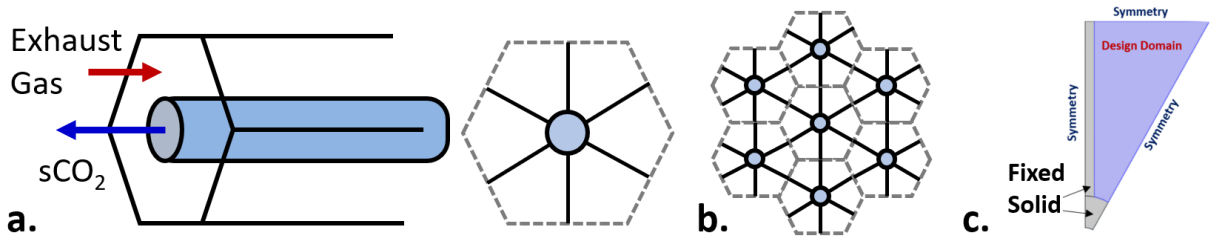

Figure 5: a. Illustrative single hexagonal unit cell (UC). **b**. Unit cells can be tessellated to thousands of instances in the HX cross-section. **b.** Sub-unit-cell (SUC) for topology optimization, with 12-way symmetry in the hexagon

For a given SUC finned surface geometry (assumed prismatic along the flow direction for now), the number of UCs patterned in the transverse plane (N_T) and length in the flow direction (L_{HX}) can be solved to satisfy the overall PHX UA and ΔP constraints.

Given the strict pressure drop requirement, relatively small anticipated unit cells, and assumed prismatic fin geometry (*i.e.*, identical in any transverse cross-section), the exhaust flow can be assumed laminar and fully developed. For these conditions, frictional pressure drop increases linearly with flow rate and overall exhaust and fin side conductance is independent of flow rate. Therefore, each 2D fin geometry has performance constants for SUC exhaust-side flow resistance $(\nabla P/\dot{m})_{ex,SUC}$ and heat transfer capacity per length $(UA/L)_{ex,SUC}$. These constants are determined from finite element conjugate heat transfer (CHT) simulations implemented in a customized workflow in COMSOL [23]. $(\nabla P/\dot{m})_{ex,SUC}$ and $(UA/L)_{ex,SUC}$ are then used to determine the number of unit cells in the transverse plane (N_T) and streamwise length (L_{HX}) needed to satisfy overall UA_{PHX} and ΔP_{max} constraints. These, in turn, determine the overall PHX mass ($M_{HX} = N_T \times L_{HX} \times (M_{UC}/L)$), which is the objective function to minimize. Here, (M_{UC}/L) is the mass of a single hexagonal UC per length.

It is argued that the minimum total mass design will be approximately the most economical to produce by additive manufacturing.

Detailed cost models have been developed for metal additive manufacturing of parts that independently account for factors including material use, machine time, labor costs, and energy [24]. Huang *et al*. [25] developed a topology optimization method for structural parts that accounts for comprehensive build costs, rather than just material use. In a case study, they demonstrated how a more massive bracket design could be produced with much lower machine time, resulting in 7% overall cost savings. Such opportunities can be found in power-bed fusion AM because borders of parts are often formed separately and at different speeds than internal solid zones, and each additional vertical layer requires a "recoating" step. Later, Ulu *et al*. [26]

applied this simultaneous structural and overall cost optimization to four different mechanical components. They found ~5% cost savings compared with optimization only considering mass. In future work, such comprehensive cost models could be integrated into the AM heat exchanger design framework proposed here, yielding comparable capital cost savings.

In the next phase of the design process, topology optimization is used to identify an optimal SUC design. Figure 6 provides a schematic of the proposed topology optimization process.

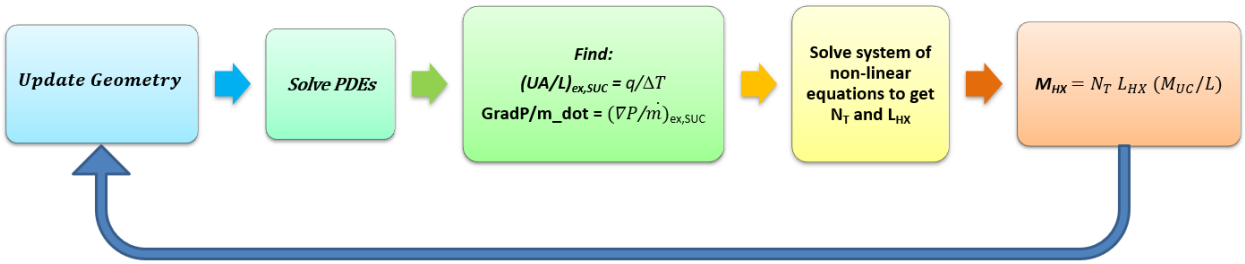

Figure 6: Flowchart for the sub-unit-cell topology optimization procedure

A distinct aspect of this design process is that the total PHX mass (or production cost) is the objective function for topology optimization, even though geometry optimization and CHT simulations are performed at the SUC-level. If, instead, optimization was performed using a local objective function based on thermal-fluid performance parameters, such as $UA_{ex,SUC}/(\nabla P/\dot{m})_{SUC}$, resulting designs may have high transport performance, but may not be economically optimal.

2.4 Topology optimization problem formulation and evaluation

Topology optimization is used to converge on fin geometries in the exhaust-gas channels of the SUCs that minimize total PHX mass while satisfying *UA* and pressure drop constraints. To initialize the process, the edge-to-edge hexagonal UC size is assumed to be 8 mm. The inner tube diameter (ID) is chosen to be 500 µm with an outer diameter (OD) of 1,500 µm. The choice of 500 µm thickness for the sCO_2 circular tube is made considering the high internal pressure and minimum wall thickness requirements of typical AM systems needed to avoid porosity. Exhaust-gas side fins are allowed to be thinner as minor porosity in those structures would not lead to PHX failure. A fixed radial fin of 500 µm thickness is included in each SUC for structural integrity of the overall PHX. The choice of the 8 mm unit cell size and single fixed fin are justified through parametric studies in Sections 2.7 and 3, respectively. To reduce the computational cost and problem complexity, a $1/12^{th}$ symmetric SUC is extracted from each hexagonal UC. These choices lead to a 30° wedge-shaped *design domain* in which the exhaust-gas-side heat transfer surfaces and flow areas can be varied through the topology optimization calculations (Figure 5c).

2.4.1 Exhaust-gas-side flow model

The exhaust flow is assumed to be steady, laminar, incompressible and locally fully developed. The laminar flow assumption is justified based on the geometry of the final optimized HX UC, which has a hydraulic diameter D_H = 1.17 mm and L_{HX}/D_H = 353. This corresponds to exhaust-gas Reynolds numbers (Re_{ex}) of 447 – 592 (varying with temperature along the flow length), which are within the laminar flow range. The locally fully-developed flow approximation is justified because the predicted laminar entrance length ($L_{ent} = 0.06 \times Re_{ex} \times D_H$) of 31 – 42 mm is approximately 10% of the total HX length of 413 mm. It should be noted that the exhaust flow properties will vary with temperature along the PHX length (~500°C – ~200°C). For laminar fully developed flow, *UA* and friction factor would only be modified by variations in gas conductivity and viscosity, which scale as $\sim T^{1/2}$ (~28% variation).

Flow blockage by the heat transfer fins is modeled with a porous media approach. To implement this effect, a Brinkman friction term is added, which imposes a resistive force proportional to velocity in solid areas, resulting in minimal penetration, as described in [27]. The resulting reduced momentum equation for pressure-driven flow in the streamwise direction is linear and given by Eqn. 5.

$$\mu_{ex}\left(\frac{\partial^2 w_{ex}}{\partial x^2}+\frac{\partial^2 w_{ex}}{\partial y^2}\right)=\gamma\frac{dP}{dz}-\bar{\alpha}(1-\gamma)w_{ex} \tag{5}$$

Here, w_{ex} is the exhaust gas streamwise velocity field, μ_{ex} is the exhaust gas viscosity, and $\frac{dP}{dz}$ is the uniform pressure gradient in the flow direction. $\bar{\alpha}$ is an absorption coefficient (inverse permeability) used to scale the Brinkman flow resistance term in solid zones. γ is the design variable field generated by the iterative topology optimization process, which varies from 0 to 1 for solid and fluid regions, respectively. Ideally, the γ field should be *sharp*, with zones of 0 (solid) and 1 (fluid) value separated by very thin transitions. However, intermediate iterations from the topology optimization algorithm may have diffuse γ fields.

A non-dimensional form of Eqn. 5 is given by Eqn. 6.

$$\left(\frac{\partial^2 w_{ex}^*}{\partial x^{*2}}+\frac{\partial^2 w_{ex}^*}{\partial y^{*2}}\right)=\gamma\frac{dP^*}{dz^*}-\overline{\alpha^*}(1-\gamma)w_{ex}^* \tag{6}$$

Here, w_{ex}^* is the non-dimensional exhaust velocity defined as $\frac{w_{ex}}{U}$, where U is a characteristic velocity. Similarly, x^*, y^*, and z^* are non-dimensional spatial variables defined as $\frac{x}{L}$, $\frac{y}{L}$, and $\frac{z}{L}$, respectively, with characteristic length L. $P^* = \frac{P-P_\infty}{\frac{\mu_{ex}U}{L}}$ is the dimensionless pressure with characteristic pressure P_∞. $\overline{\alpha^*}$ is the dimensionless inverse permeability defined as $\frac{L^2\bar{\alpha}}{\mu_{ex}}$. The maximum inverse permeability should be sufficiently large to ensure negligible flow through solid areas, but excessively large values can cause numerical instabilities. Using the non-

dimensional scaling in Eqn. 6, $\bar{\alpha}$ is chosen to be $500\times\frac{\Delta P_{max} L}{\mu_{ex} U}$, where the characteristic length L and velocity U are taken as 25 mm and 1 m s^{-1}, respectively.

The governing flow equation (6) is solved for the *design domain* portion of the SUC (Figure 5c) – the portion through which exhaust gas flows. No-slip boundary conditions are imposed on the fixed radial fin and central tube boundaries. The other SUC boundaries are symmetry planes.

Eqn. 6 is solved with representative exhaust-gas material properties ($\mu_{ex} = 3.5 \times 10^{-5}$ kg m^{-1} s^{-1}, $\rho_{ex} = 0.47$ kg m^{-3}) and an arbitrary pressure gradient. The lowest exhaust-gas side density value (at 482°C inlet) is used here to conservatively calculate the total pressure drop. The total mass flow rate is then integrated over the SUC ($\dot{m}_{ex,SUC}$). As the exhaust flow is assumed laminar and fully developed, the frictional pressure gradient is linearly proportional to the mass flow in each SUC. Therefore, a characteristic exhaust-gas flow-resistance constant can be defined for a SUC geometry. The characteristic $(\nabla P/\dot{m})_{ex,SUC}$ constant can then be used as one of the closure parameters to solve for the PHX flow length and number of unit cells (L_{HX}, N_T) to satisfy the total pressure drop constraint as given in Section 2.4.3, Eqn. 20.

2.4.2 Exhaust-gas-side heat transfer model

The thermal transport equation for steady laminar flow in the axial direction is given by Eqn. 7:

$$\rho_{ex} C_{p,ex} w_{ex} \left(\frac{\partial T_{ex}}{\partial z}\right) = k_{ex} \left(\frac{\partial^2 T_{ex}}{\partial x^2} + \frac{\partial^2 T_{ex}}{\partial y^2} + \frac{\partial^2 T_{ex}}{\partial z^2}\right) + \Phi \tag{7}$$

Here, $C_{p,ex}$ is the exhaust specific heat at constant pressure, T_{ex} is the exhaust temperature, k_{ex} is the exhaust thermal conductivity, and Φ is the volumetric viscous dissipation rate. As the exhaust gas has Pr ~ 1 (Pr = 0.698 at exhaust inlet temperature 482ºC), the hydrodynamically fully developed flow condition (Section 2.4.1) implies thermally developed flow. Further, the PHX operates in counterflow with nearly balanced thermal capacity rates ($\dot{m}C_p$) for both streams. Given these conditions, the exhaust gas temperature varies approximately linearly in the flow direction. Therefore, it can be assumed that $\frac{\partial T_{ex}}{\partial z}$ is constant and $\frac{\partial^2 T_{ex}}{\partial z^2} = 0$. Further, the high exhaust-gas side Peclet number (Pe = $\mathrm{Re_{ex}}\times\mathrm{Pr_{ex}}$ = 312 – 413) indicates that axial conduction in the fluid ($\frac{\partial^2 T_{ex}}{\partial z^2}$) is negligible compared to planar conduction ($\frac{\partial^2 T_{ex}}{\partial x^2}, \frac{\partial^2 T_{ex}}{\partial y^2}$). The thermal transport equation can therefore be reduced and non-dimensionalized to:

$$w^*_{ex} \left(\frac{dT^*_{ex}}{dz^*}\right) = \frac{1}{\mathrm{Pe}} \left(\frac{\partial^2 T^*_{ex}}{\partial x^{*2}} + \frac{\partial^2 T^*_{ex}}{\partial y^{*2}}\right) + \frac{\mathrm{Ec}}{\mathrm{Re}} \Phi^* \tag{8}$$

Here, T^*_{ex} is the non-dimensional exhaust side temperature defined as $\frac{T_{ex}-T_o}{\Delta T}$, where T_o and ΔT are a reference temperature and reference temperature difference, respectively. Φ^* is the

dimensionless volumetric viscous dissipation rate $\left(\Phi^* \frac{\Phi L^2}{U^2 \mu_{ex}}\right)$. Ec is the Eckert number defined as $\frac{U^2}{C_{p,ex}\,\Delta T}$, which is the ratio of flow's kinetic energy to representative enthalpy difference. Re $= \frac{\rho_{ex} U L}{\mu_{ex}}$ is the Reynolds number. The ratio of Eckert number to Reynolds number is very small (2.0 – 2.7×10^{-4}). This indicates that the viscous dissipation term is negligible.

The density-based topology optimization method allows the presence of both fluid and solid regions in the design domain. This can be represented in the transport equation (Eqn. 8) by varying the thermal conductivity with γ. Here, thermal conductivity is interpolated between solid and fluid values using a Rational Approximation of Material Properties (RAMP)-style function as presented in [28] and given by Eqn. 9:

$$k(\gamma) = k_{ex} \frac{\gamma\left(\frac{k_{ex}}{k_s}(1+b_k) - 1\right) + 1}{\frac{k_{ex}}{k_s}(1 + b_k\gamma)} \tag{9}$$

$k(\gamma)$ is the RAMP-style thermal conductivity, and b_k is the convexity interpolation parameter that controls the convexity of the interpolation and can be adjusted to penalize intermediate design variables with respect to effective thermal conductivity. The value of k_{ex}, k_s, and b_k are taken as 0.053 W m^{-1} K^{-1}, 30 W m^{-1} K^{-1}, and 0, respectively. The RAMP style function was selected here, instead of the Solid Isotropic Material with Penalization (SIMP) or power law forms, because it has a non-zero gradient at $\gamma = 0$. This has been found to improve convergence properties and alleviate issues with spurious low density modes in thermal-fluid problems [29]. Substituting Eqn. 9 into Eqn. 8 and neglecting the viscous dissipation term yields the final thermal convection diffusion equation for the design domain:

$$w_{ex}^* \left(\frac{dT_{ex}^*}{dz^*}\right) = \frac{1}{\mathrm{Pe}(\gamma)}\left(\frac{\partial^2 T_{ex}^*}{\partial x^{*2}} + \frac{\partial^2 T_{ex}^*}{\partial y^{*2}}\right) \tag{10}$$

Here, $\mathrm{Pe}(\gamma) = \mathrm{Re} \times \mathrm{Pr}\,(\gamma)$ where $\mathrm{Pr}(\gamma) = \frac{C_{p,ex}\mu_{ex}}{k(\gamma)}$.

The temperature of the inner tube wall boundary is set to an arbitrary fixed value. Symmetry conditions are applied on the other SUC boundaries. Solution of this equation for an input γ field and velocity solution (per the Section 2.4.1 model) yields the characteristic thermal conductance per length from the exhaust gas to the inside tube surface for the geometry: $(UA/L)_{ex,SUC}$.

2.4.3 sCO_2 side modeling and combined thermal-hydraulic analysis

The sCO_2 flows through circular channels, allowing use of analytic correlations to predict thermal resistance. Here, the sCO_2 temperature (180 – 467°C) is well above the critical value of 31.1°C, and transport properties trends are approximately gas-like. This permits assumption of approximately constant properties and use of constant-property heat transfer correlations rather than ones that correct for near-critical (pseudo-critical) flow effects. Such closure models should be selected carefully, considering applicability, when implementing this overall HX design

methodology, particularly for near-critical conditions at which transport properties vary sharply with temperature. In such cases, computations should be performed with multiple correlations to assess design sensitivity to such inputs.

Eqns. 11 and 12 are used to solve for the Reynolds number of the sCO_2 flow inside the tube.

$$A_{\mathrm{CO_2},tube} = \frac{\pi\,(\mathrm{ID})^2}{4} \tag{11}$$

$$\mathrm{Re}_{\mathrm{CO_2}} = \frac{\mathrm{ID}\left(\frac{\dot{m}_{\mathrm{CO_2}}}{N_T A_{\mathrm{CO_2},tube}}\right)}{\mu_{\mathrm{CO_2}}} \tag{12}$$

Here, $A_{\mathrm{CO_2},tube}$ is the sCO_2 tube cross-sectional area, $\mathrm{Re}_{\mathrm{CO_2}}$ is the sCO_2 side Reynolds number (~20,300), which is in the turbulent range, and $\mu_{\mathrm{CO_2}}$ is the sCO_2 dynamic viscosity (3.7×10^{-5} kg m^{-1} s^{-1} at T_4 and P_H, see Section 2.1). Current metal additive manufacturing processes produce relatively rough surfaces. Therefore, a 10 μm ($\epsilon/D_H = 2\%$) roughness is assumed for CO_2 flow calculations. For fully developed (hydrodynamically and thermally) turbulent flow in rough circular tubes, the Darcy friction factor can be predicted using the correlation of [30].

$$f = \left(-2\log_{10}\left\{\frac{\epsilon/D_H}{3.71} - \frac{1.975}{\mathrm{Re}_{\mathrm{CO_2}}}\ln\left[\left(\frac{\epsilon/D_H}{3.930}\right)^{1.092} + \frac{7.627}{\mathrm{Re}_{\mathrm{CO_2}} + 395.9}\right]\right\}\right)^{-2} \tag{13}$$

Frictional pressure drop can then be calculated for the parallel channels as:

$$\Delta P_{\mathrm{CO_2}} = \frac{1}{2} f \rho_{\mathrm{CO_2}} \left(\frac{\dot{m}_{CO_2}}{\rho_{\mathrm{CO_2}} N_T A_{\mathrm{CO_2},tube}}\right)^2 \frac{L_{HX}}{ID} \tag{14}$$

Here, $\Delta P_{\mathrm{CO_2}}$ is the sCO_2 side pressure drop, and $\rho_{\mathrm{CO_2}} = 220$ kg m^{-3} is the sCO_2 side density at T_4 and P_H. Using the above correlations, the sCO_2 side pressure drop for the final design comes out to be 218 kPa which is only 0.7% of the sCO_2 inlet pressure (P_H = 31 MPa). This confirms that the sCO_2-side frictional pressure drop is not an important consideration in this PHX design.

The rough channel Nusselt number can be calculated with the correlation of [31].

$$\mathrm{Nu}_{\mathrm{CO_2}} = \frac{\left(\frac{f}{8}\right)\left(\mathrm{Re}_{\mathrm{CO_2}} - 1000\right)\mathrm{Pr}_{\mathrm{CO_2}}}{1 + 12.7\sqrt{f/8}\left(\mathrm{Pr}_{\mathrm{CO_2}}^{2/3} - 1\right)} \tag{15}$$

Here, $\mathrm{Nu}_{\mathrm{CO_2}}$ is the sCO_2 Nusselt number, and $\mathrm{Pr}_{\mathrm{CO_2}} = 0.780$ is the sCO_2 side Prandtl number calculated at T_4 and P_H. The Nusselt number is then used to calculate the heat transfer coefficient and thermal resistance for the sCO_2 side as given be Eqns. 16 and 17, respectively.

$$\mathrm{HTC}_{\mathrm{CO}_2} = \frac{\mathrm{Nu}_{\mathrm{CO}_2} k_{\mathrm{CO}_2}}{\mathrm{ID}} \tag{16}$$

$$R_{CO_2} = \frac{1}{L_{HX}\,\pi\,\mathrm{ID}\,N_T\,\mathrm{HTC}_{\mathrm{CO}_2}} \tag{17}$$

Here, $\mathrm{HTC}_{\mathrm{CO}_2}$ is the heat transfer coefficient of the sCO_2 side, k_{CO_2} is the thermal conductivity of sCO_2 (0.060 W m^{-1} K^{-1}), and R_{CO_2} is the sCO_2 side thermal resistance.

The CO_2-side resistance can be combined with the fin and exhaust-side resistance (R_{ex}) to determine the overall UA_{PHX}.

$$R_{ex} = \frac{1}{12 L_{HX} N_T (UA/L)_{ex,\mathrm{SUC}}} \tag{18}$$

$$UA_{\mathrm{PHX}} = \frac{1}{R_{\mathrm{CO}_2} + R_{ex}} \tag{19}$$

The total exhaust-side pressure drop can be calculated as:

$$\Delta P_{ex} = \frac{\left(\frac{\nabla P}{\dot{m}}\right)_{ex,SUC} L_{HX} \dot{m}_{ex,SUC}}{12 N_T} \tag{20}$$

Eqns. 12-17 and 18-20 are simultaneously solved to find the PHX length (L_{HX}) and number of unit cells in the transverse plane (N_T) that deliver the target thermal capacity (UA_{PHX} = 225 kW K^{-1}) and exhaust-gas-side pressure drop (ΔP_{ex} = 8 kPa). These parameters can then be used to calculate total PHX mass for a given UC geometry.

2.4.4 Topology optimization process

The objective function to minimize is the total PHX mass, defined by Eqns. 21 and 22:

$$\frac{M_{UC}}{L} = 12 \rho_s A_{s,SUC} \tag{21}$$

$$M_{\mathrm{PHX}} = N_T L_{HX} \left(\frac{M_{\mathrm{UC}}}{L}\right) \tag{22}$$

Here, $A_{s,UC}$ is the total solid area in the SUC, $\rho_s = 7{,}500$ kg m^{-3} (stainless steel) is the solid density, and M_{HX} is the total mass of the heat exchanger.

SUC geometries are obtained using the COMSOL density-based topology optimization module [32]. A gradient-based solver is used because it follows a path in the design variable space where each new iteration is based on local derivative information evaluated at previously visited points. The Method of Moving Asymptotes (MMA) solver is used in this study because of its flexibility and support for problems with a large number of control variables. The analytic adjoint based gradient calculation numerical method is employed to rapidly calculate the sensitivity matrix for the optimization iterations. In each iteration, the solver generates an updated control design variable field γ_c, which represents the local gas-phase fraction.

Noise in the design variable field is reduced using a Helmholtz filter [33].

$$\gamma_f = R_{min}^2 \nabla^2 \gamma_f + \gamma_c \tag{23}$$

Here, $R_{\min}$ is the filter size, and is set to the local mesh cell size. γ_f is the filtered design variable.

The filtered design variable can have areas with intermediate values, resulting in an unphysical geometry. A hyperbolic tangent projection function [34] is therefore used to sharpen the design variable field:

$$\gamma = \frac{(\tanh\left(\beta\left(\gamma_f - \gamma_\beta\right)\right) + \tanh(\beta\gamma_\beta))}{(\tanh\left(\beta\left(1 - \gamma_\beta\right)\right) + \tanh(\beta\gamma_\beta))} \tag{24}$$

Here γ_β is the projection point, and β is the projection slope. The COMSOL default values of $\gamma_\beta = 0.5$ and $\beta = 8$ are used. γ is the final design variable field used to solve the flow and heat transfer equations.

The size of features or branches obtained from this topology optimization approach depends upon the mesh resolution. To streamline computation, the optimization procedure is initiated on a triangular coarse mesh which has few degrees of freedom and can be evaluated quickly. However, the output of this stage typically has diffuse boundaries between solid and fluid zones. The mesh is iteratively refined, initialized with the converged γ field obtained with the preceding mesh, and then solved. This process is continued until reasonably sharp and converged boundaries are achieved. In this study, one stage of mesh refinement from 1,650 to 6,460 elements in the design domain wase found to be sufficient for geometry convergence.

2.4.5 Adapting diffuse density-field geometry to manufacturable form

Even with mesh refinement, the density-function-based adjoint topology optimization solution can still yield diffuse boundaries near solid-gas interfaces (see Figure 7a). Therefore, the density-method based optimized solution for γ should be treated as a guideline that requires correction.

Here, the design variable field is exported from the topology optimization finite element solver (COMSOL) to a CAD program. Sharp boundaries between the solid and gas regions are manually traced (Figure 7b). CHT simulations are then repeated for this corrected geometry with well-defined solid and fluid regions. An extremely fine mesh is used with average element quality 0.84 and 41,864 total elements (degrees of freedom DOF = 141,983) to ensure well converged results. The exhaust flow is assumed to be steady, laminar, incompressible and fully developed as justified earlier in Section 2.4.1. Eqn. 25 provides the momentum equation solved in the wedge-shaped subdomain in Figure 7b (shown in blue). Eqn. 26 is used to solve for the gas-phase temperature field. A standard coupled conduction equation is solved for the solid subdomain.

$$\mu_{ex}\left(\frac{\partial^2 w_{ex}}{\partial x^2}+\frac{\partial^2 w_{ex}}{\partial y^2}\right)=\frac{\partial P}{\partial z} \tag{25}$$

$$\rho_{ex}c_{p,ex}w_{ex}\left(\frac{dT_{ex}}{dz}\right)=k_{ex}\left(\frac{\partial^2 T_{ex}}{\partial x^2}+\frac{\partial^2 T_{ex}}{\partial y^2}\right) \tag{26}$$

The simulations of the exact geometry provide corrected values of UC mass per length of HX (M_{UC}/L), overall UA per length per UC ($(UA/L)_{UC}$), and exhaust-side pressure gradient per mass flow rate per SUC $\left(\frac{\nabla P}{\dot{m}}\right)_{ex,UC}$. Refined values of N_T, L_T, and M_{HX} are then obtained using the algorithm described in Sections 2.4.1 – 2.4.4 (Eqns. 18-22). Values of the key output parameters ($\left(\frac{\nabla P}{\dot{m}}\right)_{ex,UC}$, $\left(\frac{UA}{L}\right)_{UC}$, $N_{T,\,L}$, M_{PHX}) differ by less than 5% between the solutions for the density-field diffuse geometry and the sharp CAD-geometry. This difference is hypothesized to be a result of minor errors in the manual tracing process.

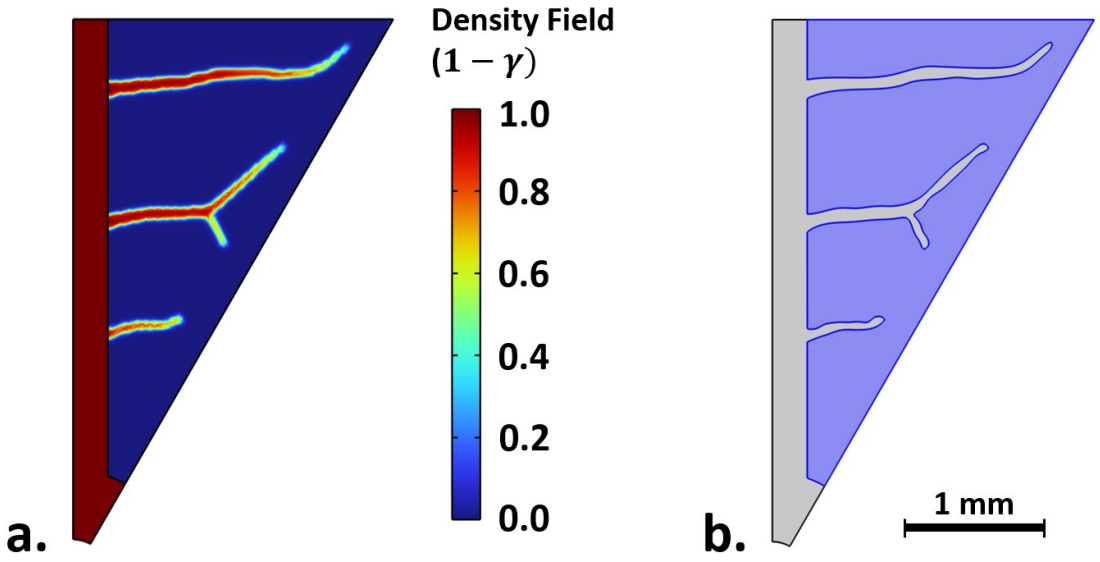

Figure 7: a. Density-field based topology optimization result (solid zones are blue, fluid zones are red). **b**. Exact geometry generated in CAD software

3 Results and analysis

3.1 Topology optimization results

The topology-optimization result obtained for a UC size of 8 mm, total pressure drop constraint of 8 kPa, and overall PHX conductance of UA_{PHX} = 225 kW K^{-1} is depicted in Figure 8.

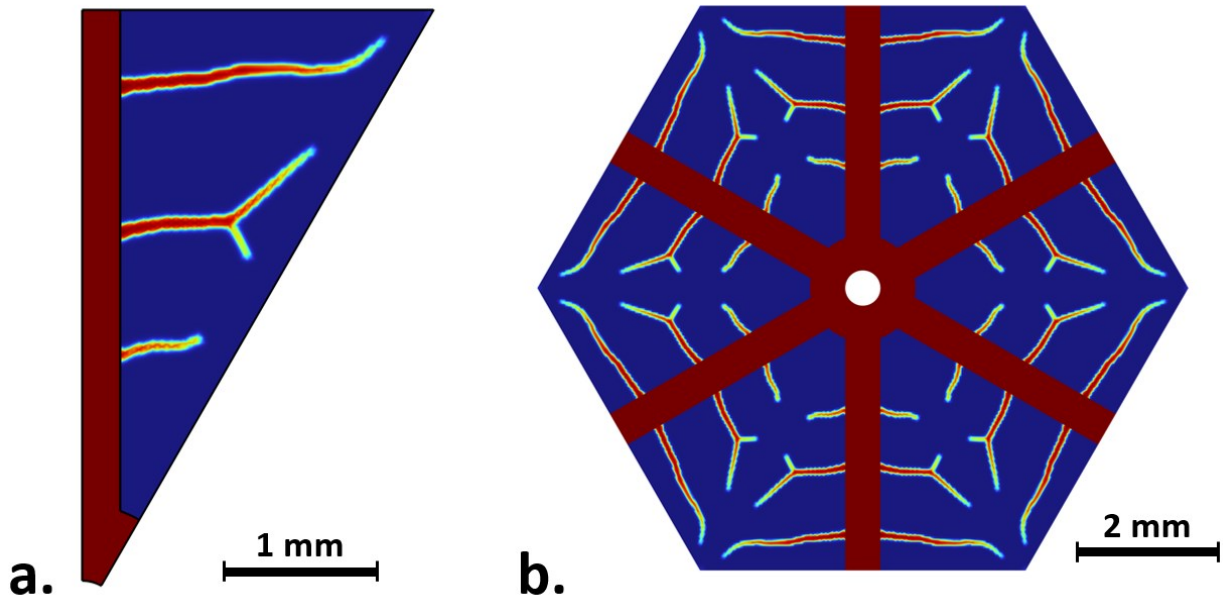

Figure 8: a. Topologically optimized SUC. Fluid zone is blue and solid zone is red.
b. Tessellation to single hexagonal UC.

Figure 9 shows the solid portion of the hexagonal UC CAD, and an illustration of multiple connected unit cells. A full PHX would contain thousands of such connected hexagonal UCs.

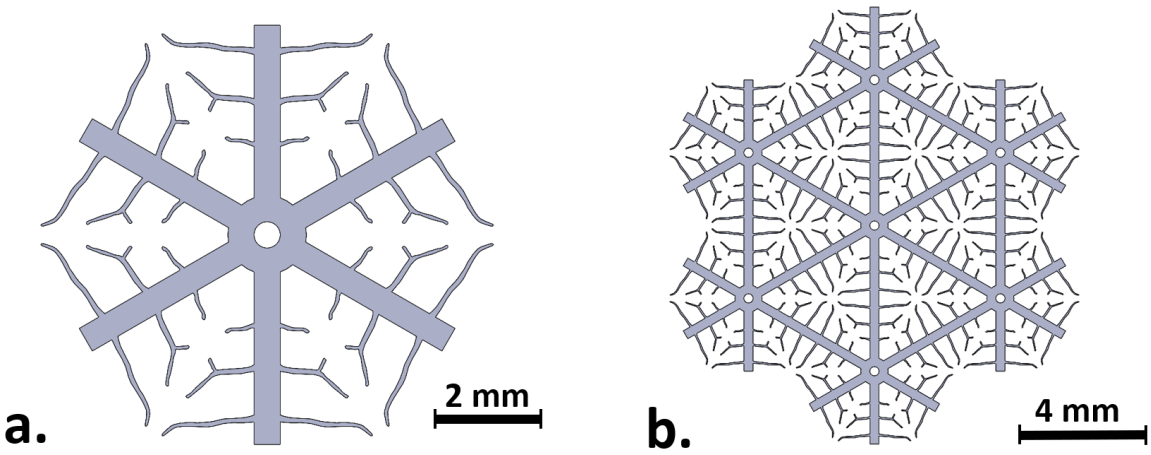

Figure 9: a. Cross section of solid hexagonal UC, **b.** Illustration of multiple connected UCs

Using the CHT analysis and solving for the parameters as discussed in Section 2.5, the final predicted mass of the stainless steel PHX, number of UCs in the transverse cross section, length, total cross-sectional area, and UC heat transfer and flow resistance parameters are summarized in Table 3. Here, $(UA/L)_{\mathrm{UC}}$ represents the total thermal resistance from the exhaust gas to sCO_2 per unit cell, per length.

Table 3: Final PHX parameters for optimized 8 mm hexagonal unit cells

M_{HX} (kg)	2,670
N_T	56,990
Frontal Area (m^2)	3.16
L_{HX} (m)	0.413
$(\boldsymbol{\nabla P/\dot{m}})_{ex,UC}$ (Pa s kg^{-1} m^{-1})	5.23×10^7
$(\boldsymbol{UA/L})_{\mathbf{UC}}$ (W m^{-1} K^{-1})	9.56

3.1.1 Optimization model verification and validation

The density-field based model adopts a number of simplifications to enable rapid evaluation of the PHX thermal-hydraulic properties and topology optimization in the large design space. The exhaust gas flow is approximated to be laminar, steady, fully developed, and at constant properties (evaluated at hot inlet state). The fins are modeled as a very-low permeability porous zone (based on γ). The local thermal conductivity in the design domain is modeled with a γ-weighted blending of gas and solid values. sCO_2 flow is modeled as constant property (evaluated at cold outlet temperature) fully developed turbulent flow using analytic friction factor and heat transfer correlations. In this section, a set of CFD models of varying fidelity are evaluated for the optimized geometry to assess the impacts of such approximations.

Main results for the density-field based model (Sections 2.4.1 – 2.4.3) analysis of the optimized geometry are summarized in Table 4. These are evaluated using exhaust gas and CO_2 properties at the PHX hot-end states ($T_{ex,in}$ = 482°C, P_{ex} = 1 atm, $T_{CO2,out}$ = 179.5°C, P_{CO2} = 31 MPa). A 2D fully developed flow analysis is performed for the manually traced CAD geometry per Section 2.4.5. This treats fins in the design space as fully solid, avoiding errors from numerical permeability and conductivity blending function. All major model outputs agree with those from the density-field model within 5%. The minor deviations are hypothesized to be due to errors in the manual tracing process. Overall, this result indicates minimal errors in the thermal-hydraulic analysis due to the density-field formulation.

Next, the sharp-boundary SUC CAD geometry is extruded to the PHX length predicted with the sharp boundary result (413.1 mm) for 3D analysis in STAR-CCM+ [35] (Figure 10). Steady, constant property 3D CFD is performed assuming laminar gas flow, RANS turbulent CO_2 flow (k-ω SST with a rough-surface wall function), and coupled solid-domain conduction. The domain is meshed with a swept method along the length of the PHX (*i.e.*, prismatic cells). Thin boundary layer cells are inserted at the wall-to-fluid interfaces. The simulation is evaluated using inlet gas and CO_2 flow rates from the 2D sharp boundary model. The case is solved with second

order discretization schemes and evaluated on systematically refined 3D meshes to obtain grid convergence. This 3D model captures effects from hydrodynamically and thermally developing flow (from uniform inlet velocity and temperature profiles) and axial conduction. Additionally, it employs a higher fidelity turbulence closure model to predict sCO_2-side transport rather than analytic correlations. The combined effects result in a 3% reduction in $(\mathrm{UA}/L)_{\mathrm{UC}}$ and 1% reduction in $(\nabla P/\dot{m})_{ex,UC}$. For this 3D analysis, $(\nabla P/\dot{m})_{ex,UC}$ is evaluated using the change in total pressure from gas inlet to outlet (*i.e.*, in terms of pressure losses).

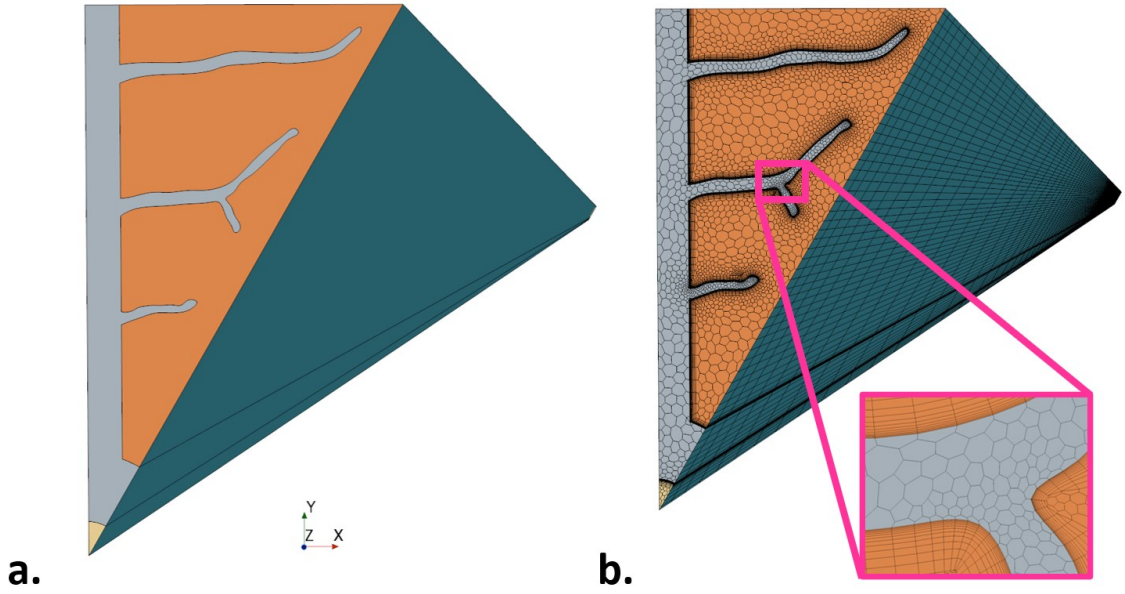

Figure 10: a. Wedge domain employed for 3D CFD study. The exhaust gas region is orange, the sCO_2 region is tan, and the solid fin region is gray. **b.** Finite volume mesh, with detail view of thin boundary layer cells near fluid-to-solid interface.

Finally, the 3D study is repeated using temperature and pressure dependent fluid properties rather than fixed values evaluated at the hot end conditions. In this case, the higher average sCO_2 Prandtl number and other minor effects yield a 9% increase in $(\mathrm{UA}/L)_{\mathrm{UC}}$. The greater average exhaust gas density significantly reduces flow velocity and frictional pressure loss, resulting in a 29% reduction in $(\nabla P/\dot{m})_{ex,UC}$.

Table 4: Comparison of PHX thermal-hydraulic metrics obtained with different simulation approaches

Metric	2D density-field model	2D sharp-boundary	3D RANS CFD (constant properties)	3D RANS CFD (Temperature-dependent properties)
$(\nabla P/\dot{m})_{ex,UC}$ (Pa s kg^{-1} m^{-1})	4.96×10^{7}	5.23×10^{7}	5.19×10^{7}	3.68×10^{7}
$(UA/L)_{\mathrm{UC}}$ (W m^{-1} K^{-1})	9.37	9.56	9.30	10.12
N_{T}	56,040	56,990		
L_{HX} (m)	0.428	0.413		
M_{HX} (kg)	2,560	2,670		

Overall, this set of simulations provides general verification for the initial 2-D density-field based PHX optimization approach. The only approximation that contributed significant errors was the use of constant fluid properties evaluated at the hot end conditions. For this optimization project, the hot end properties were selected intentionally to ensure a conservative design, as they yield the greatest $(\nabla P/\dot{m})_{ex,UC}$ and lowest $(UA/L)_{\mathrm{UC}}$. If model accuracy were deemed to be more critical, properties could have been evaluated at average temperatures or PHX calculations could have been performed with an axially segmented approach.

Additionally, an experimental study was performed for additively manufactured partial-scale (~100 W) heat exchanger coupons of similar unit-cell geometry to those presented here (see Supporting Material). That study employs heated air and pressurized water to simulate the target exhaust gas and sCO_2 streams, respectively. 2D density-field and sharp-boundary simulations were conducted for the experimentally studied unit-cell geometry. It was found that the air-side pressure drop measurements (*i.e.*, for $(\nabla P/\dot{m})_{ex,UC}$) closely matched simulation results at low Re. However, minor losses at the entrance and exits and over the tube-side plenums became significant at higher flow rates. Such effects were not considered in the sub-unit-cell simulations presented here. In future work, geometry optimization studies could be performed to minimize such losses in full heat exchangers developed with the presented approach. Simulations with both methods matched measured air-to-water heat transfer capacity values (*i.e.*, $(UA/L)_{\mathrm{UC}}$) within experimental uncertainty. Overall, this experimental study indicates general validity of the computational approaches used in this topology optimization study.

3.2 Unit cell sizing analysis

The performance of the optimized PHX with 8 mm UCs is compared with those obtained with 6, 7, and 9 mm UCs generated through the same procedure. Figure 11 shows a depiction of these topologically optimized SUCs. Table 5 provides the mass calculated by utilizing the UCs from these SUCs.

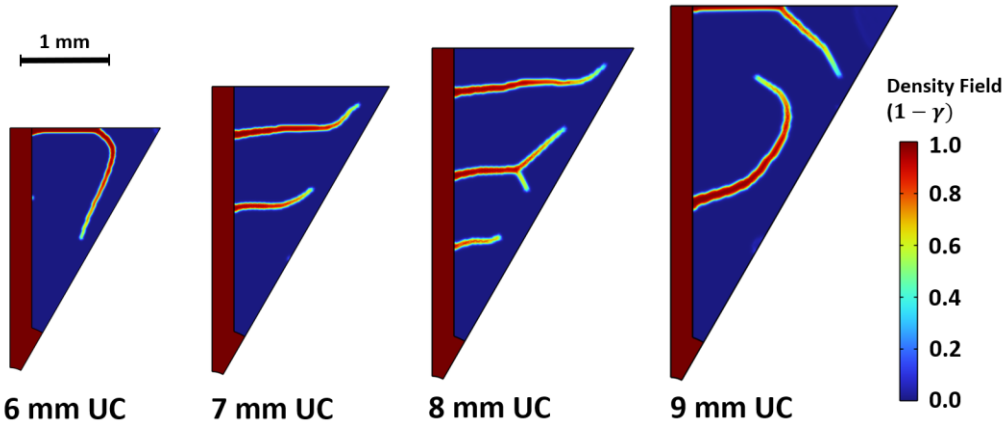

Figure 11: Topology optimization geometry results for 6 – 9 mm unit cells.

Table 5: Unit cell size vs. optimized HX parameters

	6 mm UC	**7 mm UC**	**(Baseline) 8 mm UC**	**9 mm UC**
$\boldsymbol{M}_{\mathrm{HX}}$ (kg)	2,940	2,590	**2,560**	2,830
$\boldsymbol{N}_{\mathrm{T}}$	101,000	66,460	56,040	42,760
Frontal Area (m^2)	3.15	2.82	3.11	3.00
$\boldsymbol{L}_{\mathrm{HX}}$ (m)	0.402	0.448	0.428	0.543
Bounding Volume (m^3)	1.27	1.26	1.33	1.63
$(\boldsymbol{\nabla P/\dot{m}})_{\boldsymbol{ex,UC}}$ (Pa s kg^{-1} m^{-1})	9.52×10^7	5.63×10^7	4.96×10^7	2.98×10^7
$(\boldsymbol{UA/L})_{\mathbf{UC}}$ (W m^{-1} K^{-1})	5.54	7.56	9.37	9.69

Both the smaller (6-7 mm) and larger (9 mm) UCs require greater total HX mass, suggesting that the 8 mm UC size is near-optimal for this application. The overall bounding volume is slightly lower for designs employing smaller unit cells (6 and 7 mm). This could allow use in more space constrained applications with only minor mass penalties.

3.3 System level vs. local objective functions for topology optimization

A main premise underlying this study is in the use of topology optimization objective functions formulated based on system-level considerations rather than local transport parameters. To illustrate the value of this approach, topology optimization is also performed using a representative "local" thermal-fluid objective function. For fully developed laminar exhaust flow in a SUC of given geometry, UA from the gas to the inside tube surface is independent of flow rate and frictional pressure drop is proportional to mass flow rate. Therefore, a thermal-fluid performance constant can be defined for any UC geometry:

$$\frac{(UA/L)_{ex,UC}}{(\nabla P/\dot{m})_{ex,UC}} \tag{27}$$

Optimal geometries that maximize this parameter were obtained for 4 – 8 mm hexagon SUCs following the procedure defined in Sections 2.4.4. Figure 12 presents the geometry obtained with this objective function and Table 6 provides the parameters to satisfy UA_{PHX} = 225 kW K^{-1} and ΔP_{ex} = 8.0 kPa.

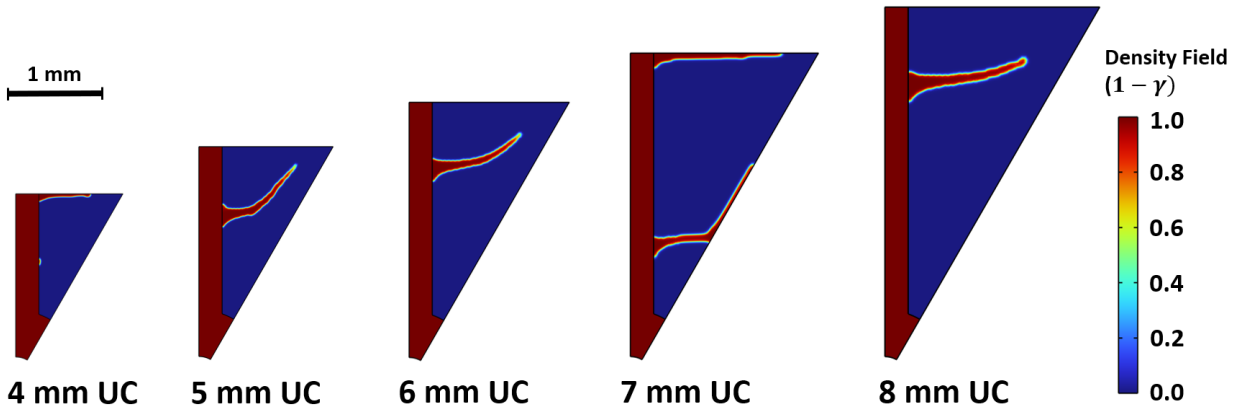

Figure 12: Local thermal hydraulic objective topology optimization geometry results for 4 – 8 mm unit cells.

Table 6: Comparison of unit cell parameters for "locally" and "globally" optimized designs

	Globally Optimized 8 mm UC	**Locally Optimized Unit Cells**				
		4 mm UC	**5 mm UC**	**6 mm UC**	**7 mm UC**	**8 mm UC**
N_T	56,040	196,450	133,930	72,930	55,350	35,300
Frontal Area (m^2)	3.11	2.72	2.90	2.27	2.35	1.94
L_{HX} (m)	0.428	0.473	0.380	0.619	0.800	1.25
Bounding Volume (m^3)	1.33	1.29	1.10	1.41	1.87	2.43
$(\nabla P/\dot{m})_{ex,UC}$ (Pa s kg^{-1} m^{-1})	4.96×10^{7}	1.58×10^{8}	1.33×10^{8}	4.47×10^{7}	2.63×10^{7}	1.06×10^{7}
$(UA/L)_{UC}$ (W m^{-1} K^{-1})	9.37	2.42	4.41	4.99	5.09	5.14
Global Objective: $\mathbf{min}(M_{HX})$ (kg)	2,560	3,910	2,950	3,190	3,970	4,330
Local Objective: $\mathbf{max}\left(\frac{(UA/L)_{ex,UC}}{(\nabla P/\dot{m})_{ex,UC}}\right)$ (kg m^3 s^{-2} K^{-1})	3.41×10^{-7}	2.68×10^{-8}	6.81×10^{-8}	1.62×10^{-7}	2.55×10^{-7}	5.70×10^{-7}

For the same UC size (8 mm), the locally optimized geometry achieves 1.7× the thermal conductance per flow resistance of the global mass optimized design. However, that geometry also requires 1.7× the mass to satisfy the global UA_{PHX} and ΔP_{ex} requirements. For this PHX design application, the poor total-mass performance of the locally optimized design occurs because the objective weighs unit cell thermal conductance and flow resistance equally. The optimization procedure converges on a relatively "open" fin structure that has very low flow resistance (~1/5 the global mass optimized design) at the cost of a 45% reduction in $(UA/L)_{UC}$.

For smaller unit cells (6 and 5 mm), the locally optimized geometries reduce total M_{PHX} to values close to those obtained from the global mass optimization approach (see Table 5). However, geometries for these smaller unit cells also have an order of magnitude lower value of

the local objective function $\left(\frac{(UA/L)_{ex,UC}}{(\nabla P/\dot{m})_{ex,UC}}\right)$. Designers focused on this local objective may seek larger UCs even though those incur significant mass penalties. Alternate local HX objective functions (as in [1], [2]) may lead to better system level performance for objectives such as HX mass/cost, total cycle efficiency, or net present value. However, the present investigation posits that the best designs for such global objectives may be obtained by employing those objectives directly, even for sub-component scale optimization.

3.4 Comparison with conventional longitudinally finned tubes

To illustrate the potential benefit of the complex PHX geometry, *conventional*-type PHX are evaluated for comparison. These only include plain radial (longitudinal) fins in the UC, and may be comparable to commercially available longitudinally finned tubes. The number and length of radial fins are varied in these designs. Figure 13 illustrates the two basic SUCs forms used for conventional designs with varying fin thickness and length.

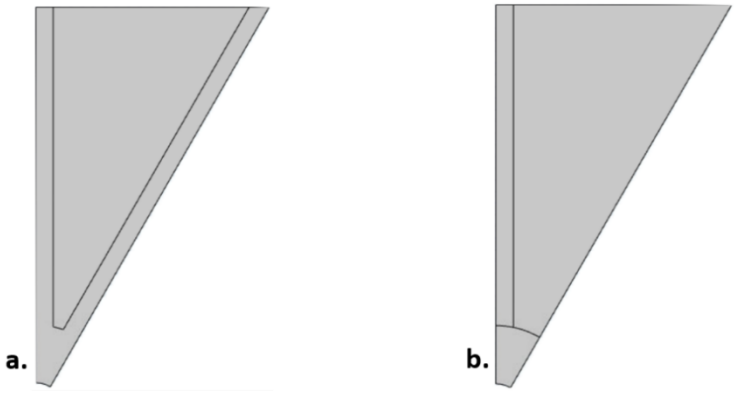

Figure 13: a. Double longitudinal fin SUC (tessellates to 12-fin UC), **b.** Single longitudinal fin SUC (tessellates to 6-fin UC)

CHT computations are performed for these geometries as in Section 2.4.5 to solve for M_{UC}/L, $(UA/L)_{ex,SUC}$, and $(\nabla P/\dot{m})_{ex,SUC}$. These values are used to obtain N_T, L_{HX} and M_{HX} for the target total PHX UA and pressure drop values (Figure 14).

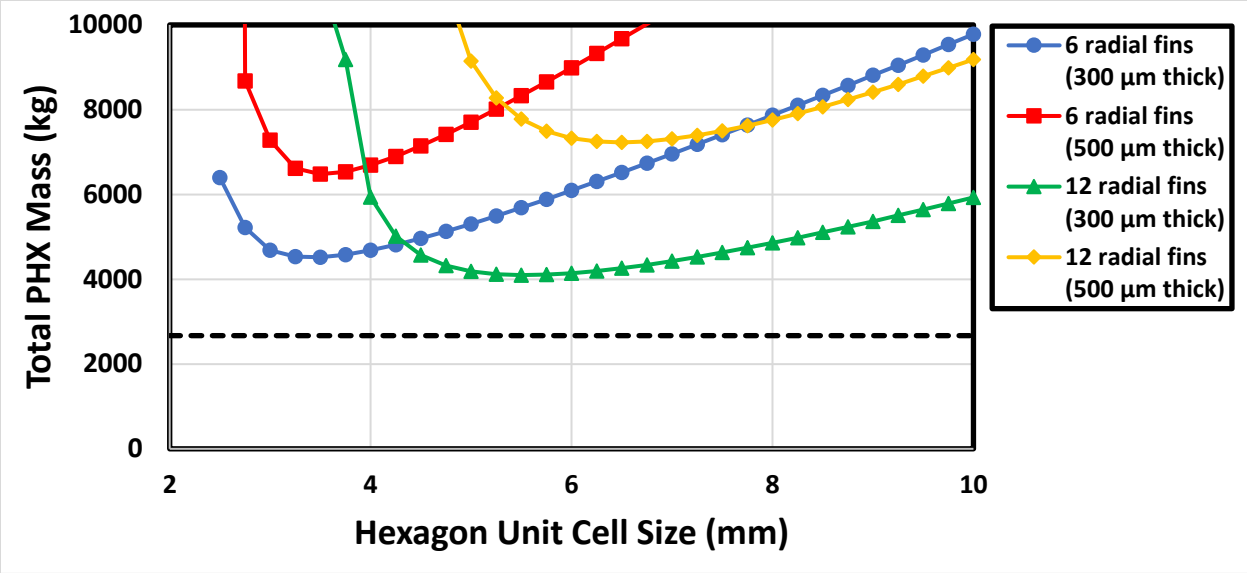

Figure 14 – Required total PHX mass to satisfy overall *UA* and exhaust pressure drop constraints for radially finned hexagonal unit cells. Results are presented for 6 and 12 evenly spaced fins of 300 µm and 500 µm thickness. The total PHX mass for the topology optimized geometry (Section 3.1) is presented with a dashed black line.

It can be seen from Figure 14 that the mass of conventional longitudinally finned heat exchangers without topology-optimization features are comparatively high. The lowest mass design identified here (12 radial fins, 300µm thick, 5.5 mm unit cell) is 4100 kg – 54% greater than obtained for the topology optimized design in Section 3.1. There is a trend toward lower PHX mass with reducing fin thickness and increased fin count, but unfeasibly thin materials may be needed to outperform the topology optimized design.

4 Conclusions

This study presents a design process for developing cost effective HXs for applications including WHR systems. The approach begins with a cycle level thermodynamic model power cycle to assess the impact of PHX *UA* and flow resistance on system efficiency. This is then coupled to an economic model that balances system efficiency (value of produced electricity) and capital costs to identify a target PHX *UA*. A high-level HX geometry template is then formed, and used as a basis for topology optimization. A 2D density-field based model is developed for optimization of PHX sub-unit cell geometries. The 2D formulation is verified for accuracy with highly resolved 3D CFD. Topology optimization is applied using a CHT physical model and an objective of minimizing total HX mass, a surrogate for capital cost. Optimization studies are performed for multiple unit cell (UC) sizes to identify a fin geometry that is hypothesized to be globally mass-optimal subject to imposed design constraints.

To illustrate the value of applying this global mass objective, an equal size (8 mm UC) geometry was developed through topology optimization seeking to maximize a local thermal-hydraulic performance measure. The design obtained using the global objective requires 38% less mass. Local-objective-based optimization for other UC sizes results in lower mass designs, but all have at least 15% greater mass than found with the global objective. Similarly, the global-mass-optimized geometry achieves 35% (or greater) reduction in HX mass compared with conventional longitudinally finned tube HXs.

The present investigation focuses on the development and theory of a PHX design process, but practicalities of fabrication have not yet been thoroughly studied. Future work is needed to assess production of such complex HXs using AM. A more detailed AM costing model should be developed and integrated. In future work, minimum AM feature sizes and actual surface roughness should be considered in the CHT and topology optimization stages. AM HXs can be experimentally tested for manufacturing defects to provide data about limitations for minimum tube wall and fin thicknesses along with allowable feature sizes. They can also be evaluated for pressure drop and hydrostatic burst strength. Moreover, topology optimization can also be applied to the sCO_2 side which may result in an even more mass efficient heat exchanger.

5 Acknowledgements

We would like to thank the US Department of Energy's Office of Energy Efficiency and Renewable Energy and Siemens Corporation for support under the research project "Flexible CHP System Utilizing Improved Gas Turbine and sCO_2 Cycles" (ORNL SAP 3400280782). We also wish to acknowledge support from the US National Science Foundation (CBET-1652578). The content in this paper is solely the responsibility of the authors and does not necessarily represent the official views of the funding organizations.

References

[1] B. S. Mekki, J. Langer, and S. Lynch, "Genetic algorithm based topology optimization of heat exchanger fins used in aerospace applications," *Int J Heat Mass Transf*, vol. 170, 2021.

[2] J. H. K. Haertel and G. F. Nellis, "A fully developed flow thermofluid model for topology optimization of 3D-printed air-cooled heat exchangers," *Appl Therm Eng*, vol. 119, pp. 10–24, 2017, doi: 10.1016/j.applthermaleng.2017.03.030.

[3] A. Gimelli, A. Luongo, and M. Muccillo, "Efficiency and cost optimization of a regenerative Organic Rankine Cycle power plant through the multi-objective approach," *Appl Therm Eng*, vol. 114, 2017, doi: 10.1016/j.applthermaleng.2016.12.009.

[4] A. H. Aslambakhsh, M. A. Moosavian, M. Amidpour, M. Hosseini, and S. AmirAfshar, "Global cost optimization of a mini-scale liquefied natural gas plant," *Energy*, vol. 148, 2018, doi: 10.1016/j.energy.2018.01.127.

[5] S. Aforkoghene Aromada, N. H. Eldrup, F. Normann, and L. E. Øi, "Simulation and Cost Optimization of different Heat Exchangers for CO2 Capture," in *Proceedings of The 61st SIMS Conference on Simulation and Modelling SIMS 2020, September 22-24, Virtual Conference, Finland*, 2021. doi: 10.3384/ecp20176318.

[6] S. G. Hall, S. Ahmad, and R. Smith, "Capital cost targets for heat exchanger networks comprising mixed materials of construction, pressure ratings and exchanger types," *Comput Chem Eng*, vol. 14, no. 3, 1990, doi: 10.1016/0098-1354(90)87069-2.

[7] Y. Zhao, H. Chen, M. Waters, and D. N. Mavris, "Modeling and cost optimization of combined cycle heat recovery generator systems," in *American Society of Mechanical Engineers, International Gas Turbine Institute, Turbo Expo IGTI*, 2003. doi: 10.1115/GT2003-38568.

[8] H. Najafi, B. Najafi, and P. Hoseinpoori, "Energy and cost optimization of a plate and fin heat exchanger using genetic algorithm," *Appl Therm Eng*, vol. 31, no. 10, 2011, doi: 10.1016/j.applthermaleng.2011.02.031.

[9] J. Wen, H. Yang, G. Jian, X. Tong, K. Li, and S. Wang, "Energy and cost optimization of shell and tube heat exchanger with helical baffles using Kriging metamodel based on MOGA," *Int J Heat Mass Transf*, vol. 98, 2016, doi: 10.1016/j.ijheatmasstransfer.2016.02.084.

[10] R. V. Rao, A. Saroj, P. Ocloń, and J. Taler, "Design Optimization of Heat Exchangers with Advanced Optimization Techniques: A Review," *Archives of Computational Methods in Engineering*, vol. 27, no. 2, 2020, doi: 10.1007/s11831-019-09318-y.

[11] F. Lange, C. Hein, G. Li, and C. Emmelmann, “Numerical optimization of active heat sinks considering restrictions of selective laser melting,” *COMSOL Conference 2018, Lausanne France*, 2018.

[12] J. Haertel, K. Engelbrecht, B. Lazarov, and O. Sigmund, “Topology Optimization of Thermal Heat Sinks,” *COMSOL conference, Grenoble Switzerland*, 2015.

[13] F. Wang, B. S. Lazarov, and O. Sigmund, “On projection methods, convergence and robust formulations in topology optimization,” *Structural and Multidisciplinary Optimization*, vol. 43, pp. 767–784, 2011, doi: 10.1007/s00158-010-0602-y.

[14] H. Kobayashi, K. Yaji, S. Yamasaki, and K. Fujita, “Freeform winglet design of fin-and-tube heat exchangers guided by topology optimization,” *Appl Therm Eng*, vol. 161, 2019, doi: 10.1016/j.applthermaleng.2019.114020.

[15] K. R. Saviers, R. Ranjan, and R. Mahmoudi, “Design and validation of topology optimized heat exchangers,” in *AIAA Scitech 2019 Forum, San Diego, CA, USA*, 2019. doi: 10.2514/6.2019-1465.

[16] S. K. Cho, M. Kim, S. Baik, Y. Ahn, and J. I. Lee, “Investigation of the bottoming cycle for high efficiency combined cycle gas turbine system with supercritical carbon dioxide power cycle,” in *Proceedings of the ASME Turbo Expo, Montreal, Quebec, Canada*, 2015. doi: 10.1115/GT2015-43077.

[17] K. Nikitin, Y. Kato, and L. Ngo, “Printed circuit heat exchanger thermal-hydraulic performance in supercritical CO2 experimental loop,” *International Journal of Refrigeration*, vol. 29, no. 5, pp. 807–814, 2006, doi: 10.1016/j.ijrefrig.2005.11.005.

[18] M. Persichilli, T. Held, S. Hostler, and E. Zdankiewicz, “Transforming Waste Heat to Power through Development of a CO2 - Based Power Cycle,” *16th International Symposium, Compressor Users-Manufacturers, Rosemount, IL, USA*, 2011.

[19] C. S. Turchi, Z. Ma, T. W. Neises, and M. J. Wagner, “Thermodynamic study of advanced supercritical carbon dioxide power cycles for concentrating solar power systems,” *Journal of Solar Energy Engineering, Transactions of the ASME*, vol. 135, no. 4, 2013, doi: 10.1115/1.4024030.

[20] A. D. Atrens, H. Gurgenci, and V. Rudolph, “Economic Optimization of a CO2-Based EGS Power Plant,” *Energy & Fuels*, vol. 25, no. 8, pp. 3765–3775, Aug. 2011, doi: 10.1021/ef200537n.

[21] R. Turton, R. C. Bailie, W. B. Whiting, J. A. Shaeiwitz, and D. Bhattacharyya, *Analysis, Synthesis, and Design of Chemical Processes, 4th Edition*. Upper Saddle River, NJ, USA: Prentice Hall, 2001. doi: 10.1016/B978-075067510-9/50032-2.

[22] A. D. Atrens, H. Gurgenci, and V. Rudolph, “Economic Optimization of a CO2-Based EGS Power Plant,” *Energy & Fuels*, vol. 25, no. 8, pp. 3765–3775, Aug. 2011, doi: 10.1021/ef200537n.

[23] "COMSOL Multiphysics® v. 5.4." www.comsol.com. COMSOL AB, Stockholm, Sweden.

[24] M. Ruffo, C. Tuck, and R. Hague, "Cost estimation for rapid manufacturing - Laser sintering production for low to medium volumes," *Proc Inst Mech Eng B J Eng Manuf*, vol. 220, no. 9, 2006, doi: 10.1243/09544054JEM517.

[25] R. Huang, E. Ulu, L. B. Kara, and K. S. Whitefoot, "Cost minimization in metal additive manufacturing using concurrent structure and process optimization," in *Proceedings of the ASME Design Engineering Technical Conference*, 2017. doi: 10.1115/DETC2017-67836.

[26] E. Ulu, R. Huang, L. B. Kara, and K. S. Whitefoot, "Concurrent Structure and Process Optimization for Minimum Cost Metal Additive Manufacturing," *Journal of Mechanical Design, Transactions of the ASME*, vol. 141, no. 6, 2019, doi: 10.1115/1.4042112.

[27] T. Borrvall and J. Petersson, "Topology optimization of fluids in Stokes flow," *Int J Numer Methods Fluids*, vol. 41, pp. 77–107, 2003, doi: 10.1002/fld.426.

[28] M. Stolpe and K. Svanberg, "An alternative interpolation scheme for minimum compliance topology optimization," *Structural and Multidisciplinary Optimization*, vol. 22, pp. 116–124, 2001, doi: 10.1007/s001580100129.

[29] O. Sigmund and K. Maute, "Topology optimization approaches," *Structural and Multidisciplinary Optimization*, vol. 48, pp. 1031–1055, 2013, doi: 10.1007/s00158-013-0978-6.

[30] U H Offor and S B Alabi, "An accurate and computationally efficient friction factor model," *Advances in Chemical Engineering Science*, vol. 6, pp. 237–245, 2016.

[31] V. Gnielinski, "New equations for heat and mass transfer in turbulent pipe and channel flow," *Int. Chem. Eng.*, vol. 16, no. 2, pp. 359–368, 1976.

[32] COMSOL Multiphysics, "Optimization Module User's Guide," 2018. https://doc.comsol.com/5.4/doc/com.comsol.help.opt/OptimizationModuleUsersGuide.pdf

[33] B. S. Lazarov and O. Sigmund, "Filters in topology optimization based on Helmholtz-type differential equations," *Int J Numer Methods Eng*, 2011, doi: 10.1002/nme.3072.

[34] F. Wang, B. S. Lazarov, and O. Sigmund, "On projection methods, convergence and robust formulations in topology optimization," *Structural and Multidisciplinary Optimization*, vol. 43, pp. 767–784, 2011, doi: 10.1007/s00158-010-0602-y.

[35] Siemens Industries Digital Software, "Simcenter STAR-CCM+ Version 16.06.008-R8." 2021.